Large Memory Window of van der Waals Heterostructure Devices Based on MOCVD-Grown 2D Layered Ge₄Se₉

Gichang Noh, Hwayoung Song, Heenang Choi, Mingyu Kim, Jae Hwan Jeong, Yongjoon Lee, Min-Yeong Choi, Saeyoung Oh, Min-kyung Jo, Dong Yeon Woo, Yooyeon Jo, Eunpyo Park, Eoram Moon, Tae Soo Kim, Hyun-Jun Chai, Woong Huh, Chul-Ho Lee, Cheol-Joo Kim, Heejun Yang, Senugwoo Song, Hu Young Jeong, Yong-Sung Kim, Gwan-Hyoung Lee, Jongsun Lim, Chang Gyoun Kim, Taek-Mo Chung,* Joon Young Kwak,* and Kibum Kang*

Van der Waals (vdW) heterostructures have drawn much interest over the last decade owing to their absence of dangling bonds and their intriguing low-dimensional properties. The emergence of 2D materials has enabled the achievement of significant progress in both the discovery of physical phenomena and the realization of superior devices. In this work, the group IV metal chalcogenide 2D-layered Ge_4Se_9 is introduced as a new selection of insulating vdW material. 2D-layered Ge_4Se_9 is synthesized with a rectangular shape using the metalcorganic chemical vapor deposition system using a liquid germanium precursor at 240 °C. By stacking the Ge_4Se_9 and MoS_2, vdW heterostructure devices are fabricated with a giant memory window of 129 V by sweeping back gate range of ±80 V. The gate-independent decay time reveals that the large hysteresis is induced by the interfacial charge transfer, which originates from the low band offset. Moreover, repeatable conductance changes are observed over the 2250 pulses with low non-linearity values of 0.26 and 0.95 for potentiation and depression curves, respectively. The energy consumption of the MoS_2/Ge_4Se_9 device is about 15 fJ for operating energy and the learning accuracy of image classification reaches 88.3%, which further proves the great potential of artificial synapses.

1. Introduction

Van der Waals (vdW) heterostructure devices can exert many interesting physical phenomena,[1–7] such as exciton dynamics,[8] interfacial charge transfer,[9,10] and the superconductivity in moiré structures.[11] Recently, the density functional theory (DFT)-based high-throughput computations have predicted that there are more than a thousand candidate crystals could possibly exist in the form of 2D layered materials (2DLM).[12] However, fewer than a hundred 2DLM among the candidate materials are available to synthesize. Therefore, there are still many opportunities to discover new 2DLM, and various combinations of vdW heterostructures can be generated from the new 2DLM through vdW stacking. For device applications implementing these vdW heterostructures, the engineering of the band offset that is created at the junction of

G. Noh, H. Song, M. Kim, M.-k. Jo, E. Moon, T. S. Kim, H.-J. Chai, K. Kang
Department of Materials Science and Engineering
Korea Advanced Institute of Science and Technology (KAIST)
Daejeon 34141, Korea
E-mail: kibumkang@kaist.ac.kr
G. Noh, D. Y. Woo, Y. Jo, E. Park, J. Y. Kwak
Center for Neuromorphic Engineering
Korea Institute Science and Technology (KIST)
Seoul 02792, Korea
E-mail: jykwak@kist.re.kr
H. Choi, J. Lim, C. G. Kim, T.-M. Chung
Thin Film Materials Research Center
Korea Research Institute of Chemical Technology (KRICT)
Daejeon 34114, Korea
E-mail: tmchung@krict.re.kr

J. H. Jeong
Department of Materials Science and Engineering
Yonsei University
Seoul 03722, Korea
Y. Lee, H. Yang
Department of Physics
Korea Advanced Institute of Science and Technology (KAIST)
Daejeon 34141, Korea
M.-Y. Choi, C.-J. Kim
Department of Chemical Engineering
Pohang University of Science and Technology (POSTECH)
Pohang 37673, Korea
S. Oh, H. Y. Jeong
Graduate School of Semiconductor Materials and Devices Engineering
Ulsan National Institute of Science and Technology (UNIST)
Ulsan 44919, Korea
M.-k. Jo, S. Song
Operando Methodology and Measurement Team
Korea Research Institute of Standards & Science (KRISS)
Daejeon 34113, Korea

adjacent materials is important,[2,5,6,13,14] as the optoelectrical properties of the vdW heterostructure device, such as the carrier mobility, subthreshold swing, and recombination rate, can be modulated depending on the range of the band offset.[15–20] Indeed, the band offset engineering has already been applied to conventional devices, such as the 2D electron gas (2DEG), photodetector, and solar cell.[21–24] In this regard, establishing the library of the 2D vdW material group serves an indispensable role in not only expanding the band offset spectrum but also bridging the various approaches for device applications beyond fundamental material research.

Meanwhile, the group-IV metal chalcogenide family (group-IV metal = Ge, Sn/chalcogen = S, Se, Te) has been actively reported as a wide bandgap 2D vdW material over the last few years.[25–27] In particular, the GeSe and $GeSe_2$ phases exhibited interesting material characteristics,[28–31] such as magnetism,[32] ferroelectricity,[33,34] thermoelectricity,[35] and nonlinear optics,[36] and could be potentially used in photonics and electronics applications, including in ovonic threshold switch devices.[37–40] According to the band structure calculation for the germanium selenide phases, Ge_4Se_9, which has not been reported to grow in 2D vdW form yet, remains an interesting material as it exhibits a small band offset with MoS_2, which is the major channel material for 2D heterostructure devices. This small band offset for the vdW heterostructure device can induce an interfacial charge transfer with a large hysteresis window. As a result, Ge_4Se_9 can be expected to serve as an important building block for the design of vdW heterostructure devices' functions based on band offset engineering, including artificial synaptic devices with a large dynamic range and linear weight tunability.

Here, we report upon the synthesis of the new phase of 2D vdW material, Ge_4Se_9, by using metal–organic chemical vapor deposition (MOCVD). In order to realize the new phase Ge_4Se_9 growth, which can be stabilized at a low temperature, we designed precursors for MOCVD that can be decomposed at a low temperature with high steric hindrance. To explore the functionality of Ge_4Se_9, we demonstrated a vdW heterostructure device with MoS_2, and surprisingly, it showed a giant hysteresis window of 129 V by sweeping a back-gate voltage at

±80 V in a different direction. Due to the low conduction band offset between MoS_2 and Ge_4Se_9, the interfacial charge transfer was induced, resulting in large hysteresis behavior with linear gate-tunability, which was also verified by the theoretical model and experiment results. Last, in order to exploit the charge transfer of the MoS_2/Ge_4Se_9 vdW heterostructure, we demonstrated bioinspired synaptic behaviors with the device including potentiation and depression curves with excellent non-linearity values ($v_{po} = 0.26$ and $v_{de} = 0.95$). In particular, the long-term plasticity after short-time decay within sub-seconds implies that the MoS_2/Ge_4Se_9 vdW heterostructure device can exert both volatile and non-volatile memory properties, which could be applied to a multifunctional memory related to associative learning.[41,42] The energy consumption of MoS_2/Ge_4Se_9 vdW heterostructure device as an artificial synapse was estimated to be 15 fJ for updating and 40 fJ for reading energy, which are similar to the typical biological synapse energy consumption per event. Based on the outstanding synaptic device performance, we conducted MNIST handwritten image classification. The learning accuracy reached 88.3%, which is comparable to the ideal case.

2. Results and Discussion

2.1. Low-Temperature Growth of 2D-Layered Ge_4Se_9

Figure 1a shows the crystal structures of $GeSe_2$ and Ge_4Se_9, respectively. Ge_4Se_9 is a slightly Se-rich phase compared to $GeSe_2$, and the two phases have the similar structure in the main frame of $GeSe_4$ tetrahedral. While $GeSe_2$ consists of 50% edge-sharing tetrahedral and 50% corner-sharing tetrahedral; by contrast, Ge_4Se_9 consists of only corner-sharing components, as the edge-shared portions of $GeSe_2$ are changed to Se–Se corner shared components.[43,44] According to the phase diagram (Figure S1a, Supporting Information),[43] Ge_4Se_9 decomposes into $GeSe_2$ and changes into a liquid phase at 385 ± 5 °C, which implies that the Ge_4Se_9 requires a lower temperature than $GeSe_2$.

Figure 1b shows a schematic of the MOCVD system of the Ge–Se compound. The two-zone heating system in our MOCVD reactor allows us to control the precursor decomposition at the first heating zone (T_1) and separately synthesize the crystal at the second heating zone (T_2). $Ge(dmamp)_2$ and dimethyl selenide $(CH_3)_2Se$ were used as Ge and Se precursors, respectively, while muscovite mica served as the substrate. We maintained the T_1 of 480 °C in order to decompose the precursors, and adjusted the temperature of T_2 to manipulate the phase of the Ge–Se compound: a high temperature of 400 °C for $GeSe_2$ and a low temperature of 240 °C for Ge_4Se_9. The change in the morphology of the Ge–Se compound can be observed from Ge_4Se_9, which comes in the form of a rectangular shape, all the way to $GeSe_2$, which forms a rhombus shape at the range of temperature of T_2 from 240 to 400 °C, as shown in Figure S2, Supporting Information.

First, we characterized our Ge_4Se_9, grown at a T_2 temperature of 240 °C. The optical reflectance image in Figure 1c shows that Ge_4Se_9 has thin 2D crystals with a rectangular shape with sharp facets. The flat surface and sharp edges were confirmed

W. Huh, C.-H. Lee
KU-KIST Graduate School of Converging Science and Technology
Korea University
Seoul 02841, Korea

C.-H. Lee
Advanced Materials Research Division
Korea Institute of Science and Technology (KIST)
Seoul 02792, Korea

Y.-S. Kim
Low-Dimensional Material Team
Korea Research Institute of Standards and Science (KRISS)
Daejeon 34113, Korea

G.-H. Lee
Department of Materials Science and Engineering
Seoul National University
Seoul 08826, Korea

J. Y. Kwak
Division of Nanoscience and Technology
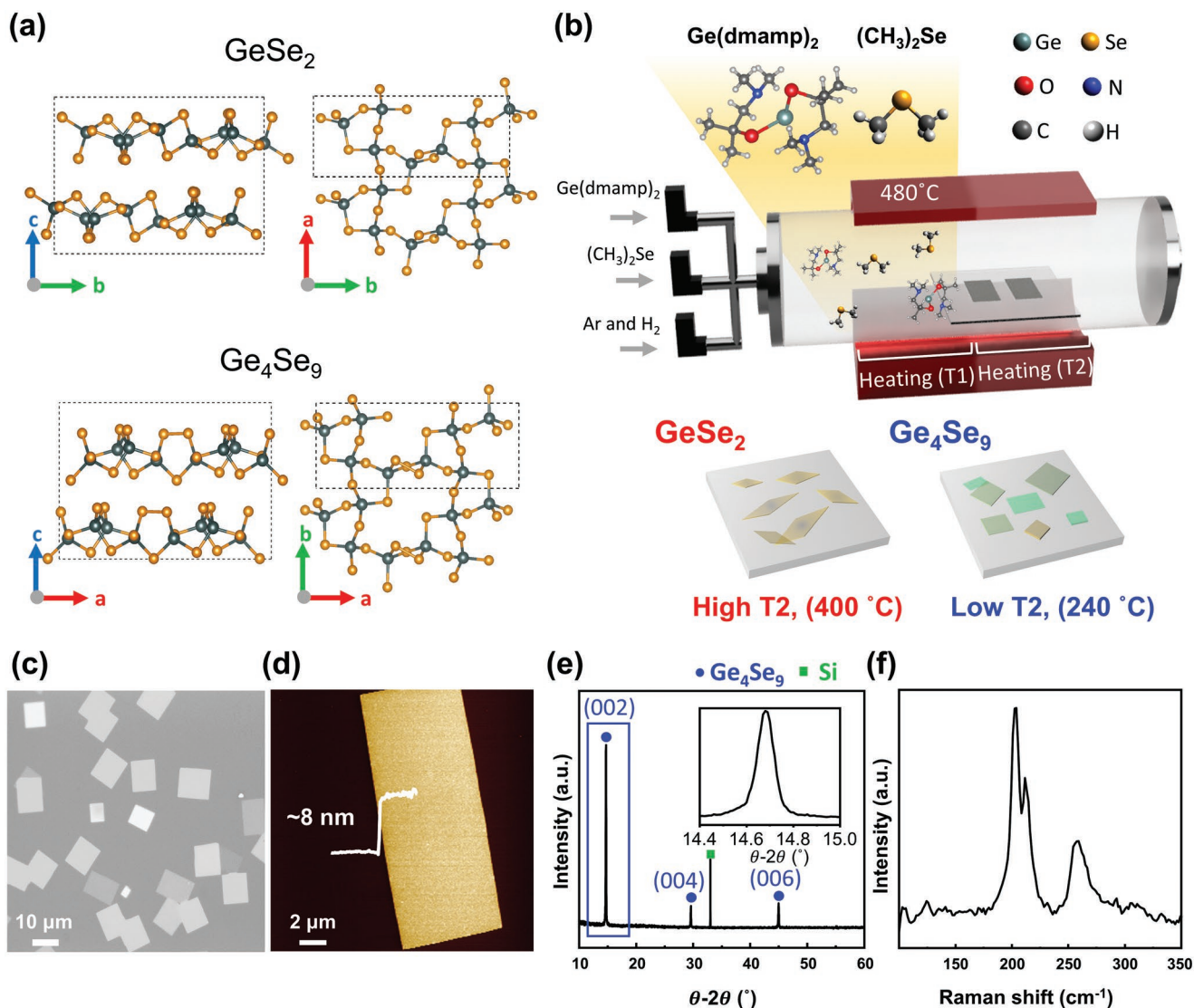Korea University of Science and Technology (UST)
Daejeon 34113, Korea

Figure 1. Growth of the Ge–Se compound. a) Crystal structure of $GeSe_2$ and Ge_4Se_9. The dashed line represents the unit cell of crystal. b) Schematics of the MOCVD method with temperature-dependent Ge–Se phase modulation, ($GeSe_2$: 400 °C, Ge_4Se_9: 240 °C). c) Optical reflectance image of Ge_4Se_9 flakes on mica substrate. d) AFM image of Ge_4Se_9 with 7 nm height. e) XRD measurement of Ge_4Se_9. The inset shows magnified graph of the (002) peak. f) Raman spectrum of Ge_4Se_9.

by the atomic force microscopy (AFM) image in Figure 1d. The thickness of the as-synthesized flakes ranged from 5 to 50 nm, depending on the conditions of growth temperature and growth time. Figure 1e shows the X-ray diffraction (XRD) pattern of rectangular flakes after the grown Ge_4Se_9 on the mica substrate was dry transferred to a SiO_2/Si substrate. The flake peaks were well matched with the orthorhombic Ge_4Se_9 (JCPDS 01-073-3670)[44] with a distinct peak (14.67°) belonging to the (002) crystal plane. In addition, the observed group of (001) plane direction peaks indicates that our grown Ge_4Se_9 is well aligned in the c-axis directions. Figure 1f shows the Raman spectrum of the as-grown flake. The Raman scattering bands at 198 and 214 cm^{-1} were due to the Ge—Se bonding, and the scattering band of 260 cm^{-1} was due to the Se–Se dimer.[45] The $GeSe_2$ was grown when the T_2 was heated at 400 °C. The optical reflectance image and the AFM image in Figure S3, Supporting

Information, show the uniform distribution of a rhombic structure with a sharp facet. The XRD pattern is consistent with $GeSe_2$ (JCPDS-01-071-0177), and the prominent peak (210 cm^{-1}) in the Raman spectrum exhibits the out-of-plane A_g mode of $GeSe_2$.

The Ge_4Se_9 phase was further investigated using transmission electron microscopy (TEM). The orthorhombic structure of the grown material was observed through a selected-area electron diffraction (SAED) pattern and energy-dispersive X-ray spectroscopy (EDX) analyses. **Figure 2**a shows a low-magnification, high-angle annular dark-field scanning transmission electron microscopy (HAADF-STEM) image of the Ge_4Se_9 flake. The high-resolution TEM (HR-TEM) image was shown in Figure S4, Supporting Information, which exhibited a precisely ordered nature without the segregation of different phases or dislocations in the Ge_4Se_9 crystal. The SAED
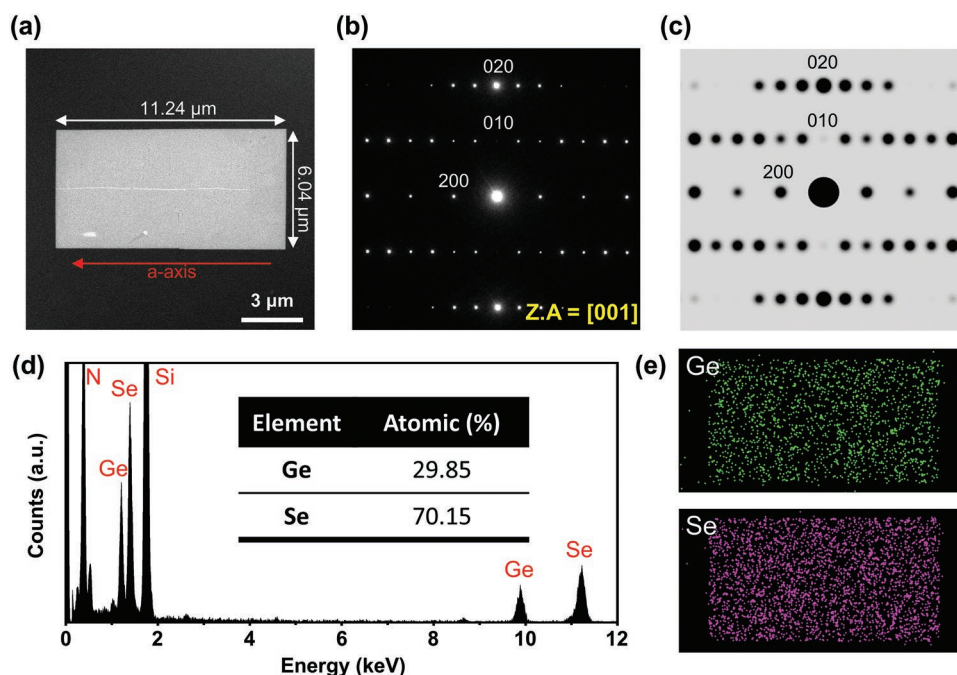
Figure 2. Characterizations of few-layer Ge_4Se_9. a) Low-magnification STEM image of Ge_4Se_9, and b) the corresponding SAED pattern. c) Simulated electron diffraction pattern of Ge_4Se_9 taken along the [001] zone axis. d) EDX spectrum obtained from a Ge_4Se_9 in (a). The inset table exhibits the elemental ratio of Ge and Se. The Si and N originated from SiN TEM grid. e) Ge and Se EDX mapping images.

pattern in Figure 2b exhibits sharp diffraction spots, which indicate a single-crystal structure with high crystallinity of the flake. Additionally, the SAED pattern of the TEM result was consistent with the simulated electron diffraction pattern seen in the Ge_4Se_9 crystal structure (Figure 2c). According to the SAED pattern results, the Ge_4Se_9 had an orthorhombic crystal with two orthogonal interlayer d-spacings of 9.0 and 7.018 Å, which can be assigned to the (200) and (010) planes that can be observed along the <001> zone axis. These values were also well matched with the interplanar spacing of Ge_4Se_9. Compared with Figure 2a,b, the long side of the rectangular flake is the [100] direction where the Se—Se bonding exists. The elemental ratio of Ge_4Se_9 was confirmed by the EDX spectrum. In the EDX spectrum of Figure 2d, the Si and N peaks originate from the SiN TEM grid, and the measured ratio of Ge and Se is about 4:9, which is consistent with the stoichiometry of Ge_4Se_9. The uniform distribution of Ge and Se can also be seen in Figure 2e. The binding energy of Ge 3d, Se 3d5/2, and Se 3d3/2 peaks are also indicated in Figure S1b,c, Supporting Information, by X-ray photoelectron spectroscopy (XPS). These peaks indicate the +4 oxidation state of Ge and the −2 oxidation state of Se, and the elemental ratio of Ge and Se by EDX was 29.85:70.15, which is similar to the 4:9 ratio of Ge_4Se_9.[45] Additionally, we obtained the similar results (31.16:68.84) of the elemental ratio by XPS.

We assume that the kinetics-driven two-zone MOCVD system and the low-reactive precursor enable the synthesis of 2D-layered Ge_4Se_9. The decomposed germanium precursor migrated to the growth zone through lateral gas flow, and the homogenous nucleation of Ge–Se proceeded under the Si-rich environment. In particular, it can reach the growth zone with lower chemical reaction and, simultaneously, create a Si-rich

environment due to the low reactivity of the precursor.[46,47] Furthermore, based on phonon-free energy calculation, Ge_4Se_9 is stable at temperatures below 327 °C and $GeSe_2$ is stable above 327 °C (more details in the Note SI, Supporting Information). Thus, $GeSe_2$ could be grown at a high temperature of T_2 (400 °C), and Ge_4Se_9 could be grown at a low temperature of 240 °C.

The thickness of Ge_4Se_9 flakes can be controlled by the growth temperature and time of the second heating zone (T_2). As shown in Figure S5, Supporting Information, Ge_4Se_9 became thicker with the increase of either the growth temperature or time, respectively. This is because the dominant thermodynamic reaction with high-saturated reactants at high temperature and sufficient growth reaction time cause Ge_4Se_9 to be thicker. Furthermore, we confirmed that the epitaxial growth of Ge_4Se_9 can be possible in mica substrate, which expands the perspective of the feasibility for wafer-scale single-crystal growth of Ge_4Se_9 (details in Note SII, Supporting Information).

From these results, we successfully synthesized the 2D-layered Ge_4Se_9 within a stable phase based on the low-reactive germanium precursor using the MOCVD system at a low temperature of 240 °C. Through the manipulation of the temperature of the growth zone (T_2), we can induce the phase-selective growth of the Ge–Se compound among $GeSe_2$ and Ge_4Se_9. Our first successful growth of 2D-layered Ge_4Se_9 suggests a new guide for Ge–Se compound synthesis with easy integration for various 2D materials. Additionally, from the point of view of the thermal budget, the low growth temperature (240 °C) holds another advantage for its compatibility and applicability with other conventional fabrication processes.[48,49]

**ADVANCED
SCIENCE NEWS**
www.advancedsciencenews.com

**ADVANCED
MATERIALS**
www.advmat.de

2.2. Giant Hysteresis Window of MoS₂/Ge₄Se₉ vdW Heterostructure Device

Using the Ge_4Se_9 as a building block of the vdW heterostructures, we demonstrated MoS_2/Ge_4Se_9 vdW heterostructure devices in **Figure 3**. First, the MOCVD-grown Ge_4Se_9 was transferred onto a degenerated n-doped Si substrate with a 300 nm SiO_2 layer, followed by stacking the exfoliated multilayer MoS_2 on the MOCVD-grown Ge_4Se_9 flake using the dry transfer method. The details of the device fabrication are further explained in the Experimental Section. A drain voltage (V_{ds}) was applied to the MoS_2 channel, and a back-gate voltage was applied through the SiO_2/Si substrate (Figure S6, Supporting Information). In Figure 3b, the device exhibits typical n-type FET behavior with an on/off ratio of about 10^5. In particular, the hysteresis window (ΔV_{th}) of our device showed about 66.5 V after sweeping the back-gate voltage in the ±50 V range in a different direction (Figure 3b). To investigate the reliability of the large hysteresis of the MoS_2/Ge_4Se_9 vdW heterostructure device, we compared 12 different devices and confirmed that the average ΔV_{th} value was 64.5 V at the same sweeping voltage of ±50 V (Figure S7a,b, Supporting Information). It should be noted that the ON/OFF ratio and ΔV_{th} were still maintained after 4 weeks without significant degradation, and the device exhibited repeatable transfer curves for 300 cycles (Figure S7c,d, Supporting Information). Moreover, the hysteresis window increased linearly with different sweeping ranges of the back-gate voltage, and the maximum value of ΔV_{th} reached upto 129 V at the ±80 V sweeping range, as shown in Figure 3c. In order to confirm the robustness of the device, we also measured the endurance of the switching process between SET and RESET, as shown in Figure 3d. The current levels of the ON and OFF states were observed to be ≈10^{-7} to 10^{-12} A, with +50 V for programming and −50 V for erasing at 0.1 V read voltage, respectively. The device exerted great stability over 2000 switching cycles, while maintaining an on/off ratio of about 10^5.

In previous studies, the hysteresis behavior of MoS_2 FETs was frequently observed, and it is known that the origin of the hysteresis can be attributed to charge trapping and de-trapping processes. The absorption of H_2O and oxygen molecules from the air at the MoS_2 surface can be one possible reason.[50–52] In addition, charge trapping or de-trapping at the interface between the MoS_2 and the dielectric layer[9,10,53–56] or intrinsic defects in MoS_2[57–59] can also cause hysteresis. To study the origin of the large hysteresis window (129 V at ±80 V sweep range) of our MoS_2/Ge_4Se_9 vdW heterostructure device, we fabricated additional devices—a Ge_4Se_9 channel-only FET device and multilayer MoS_2 channel-only FET device—for use in the control experiments. As shown in Figure S8a,b, Supporting Information, the Ge_4Se_9 channel-only FET device shows an insulator property for the current range below ≈10^{-12} A. Th indicates that Ge_4Se_9 is not the main channel for current flow in
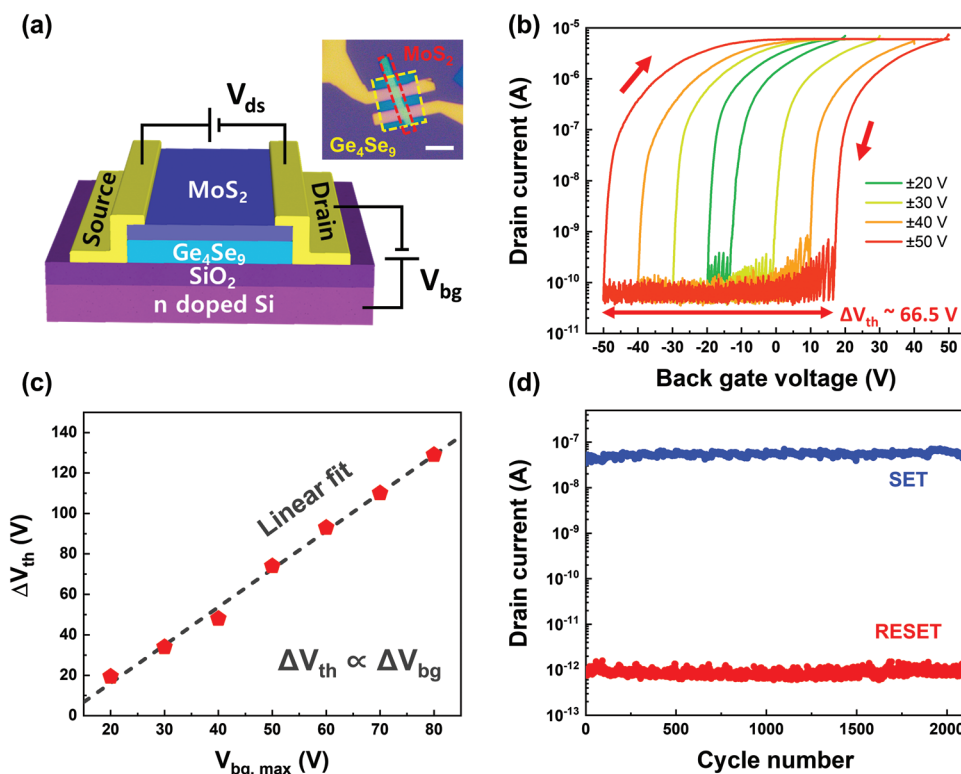

Figure 3. Electrical characteristics of the MoS_2/Ge_4Se_9 vdW heterostructure device. a) Schematic and optical microscopy image of the MoS_2/Ge_4Se_9 vdW heterostructure device with back gate applied through the SiO_2/n-doped Si substrate. MoS_2 and Ge_4Se_9 are marked by the green and yellow dashed line, respectively. Scale bar of the inset: 10 µm. b) Transfer curves of the device under the different back gate voltage sweep from ±20 to ±50 V at $V_{ds} = 0.5$ V. The threshold shift (ΔV_{th}) is about 66.5 V at the ±50 V sweeping range. c) ΔV_{th} changes with different back gate voltage ranges. The gray dashed line is fitted to the linear function. d) Endurance of the device between SET and RESET ($V_{bg} = ±50$ V) process at $V_{ds} = 0.1$ V, $V_{bg} = 0$ V.

the MoS$_2$/Ge$_4$Se$_9$ vdW heterostructure device. Additionally, the transfer curve of the multilayer MoS$_2$ channel-only FET device without Ge$_4$Se$_9$ exhibits small hysteresis behavior, as shown in Figure S8c, Supporting Information, meaning that the large hysteresis in the MoS$_2$/Ge$_4$Se$_9$ vdW heterostructure device does not stem from intrinsic defects in MoS$_2$. Last, we measured the device at the 10 mTorr vacuum condition to investigate the effects of H$_2$O and oxygen molecules in the air on large hysteresis. As shown in Figure S8d, Supporting Information, there are no dominant changes between the air and vacuum conditions, so we can exclude the gas absorption effect.

It is also known that the surface effects, such as the dangling bond on SiO$_2$, can also be another reason for the origin of hysteresis.[52–54] In order to confirm that we also fabricated additional top-gate devices: i) a MoS$_2$/Ge$_4$Se$_9$ vdW heterostructure device with h-BN (non-dangling bond 2D material with a wide bandgap (≈6 eV) as a gate dielectric layer; ii) a MoS$_2$/Ge$_4$Se$_9$ vdW heterostructure device without h-BN; and iii) a MoS$_2$-only device with h-BN as a gate dielectric layer; and then performed the comparison experiments, as shown in Figure S9, Supporting Information. It is worth noting that large hysteresis was still observed in the top-gate h-BN/Ge$_4$Se$_9$/MoS$_2$ device, whereas there was small or no hysteresis in both the MoS$_2$/Ge$_4$Se$_9$ top-gate device and MoS$_2$/h-BN top-gate device. Additionally, we investigated the effect of Ge$_4$Se$_9$ thickness

on hysteresis induced by the charge traps through defects in the body of Ge$_4$Se$_9$. We compared with the hysteresis in different thicknesses of Ge$_4$Se in the range between ≈15.51 and 45.06 nm. As shown in Figure S10, Supporting Information, the hysteresis tends to decrease as the thickness of Ge$_4$Se$_9$ increases, indicating that the defects in the body of Ge$_4$Se$_9$ were not the dominant factor for the large hysteresis behavior. From all these results, we can strongly assume that Ge$_4$Se$_9$ plays a key role as a charge trap layer in inducing hysteresis behavior, but not in the defects in the body of Ge$_4$Se$_9$.

Together with the verification of Ge$_4$Se$_9$ as a charge transfer layer, we further investigated the mechanism of the charge transfer of the MoS$_2$/Ge$_4$Se$_9$ vdW heterostructure device. From the UV–Vis absorption spectrum, the bandgap of the grown Ge$_4$Se$_9$ was measured as 2.7 eV (**Figure 4**a), which is close to the DFT calculation result of 2.5 eV, shown in Figure S17a, Supporting Information. The work function and electron affinity were estimated by UV photoelectron spectroscopy and Kelvin probe force microscopy, respectively, as shown in Figure S17c, Supporting Information and Figure 4a (right). Details of the band diagram characterization of Ge$_4$Se$_9$ are further explained in Note SIII, Supporting Information. Figure 4b summarizes the complete band diagram model of the MoS$_2$/Ge$_4$Se$_9$ vdW heterostructure.

When a positive gate voltage is applied, the Ge$_4$Se$_9$ band tilts in proportion to the edges of the gate sweep range, and the
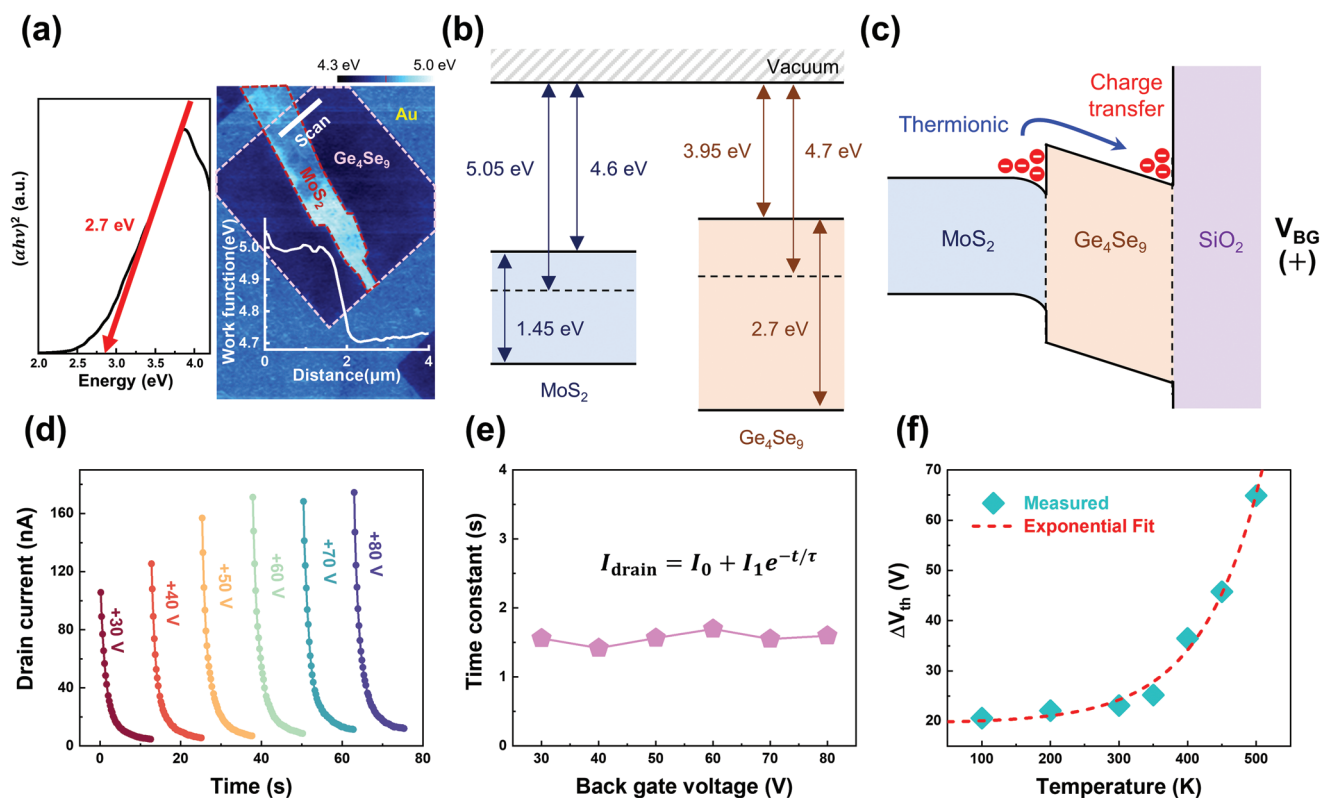

Figure 4. Charge-transfer mechanism of the MoS$_2$/Ge$_4$Se$_9$ vdW heterostructure device. a) Estimated bandgap and work function of Ge$_4$Se$_9$. The UV–Vis absorption spectrum and corresponding Tauc plot of the Ge$_4$Se$_9$ (left), and the work function mapping by KPFM (right). Inset: the line profile (white) of the work function. b) Band diagram of MoS$_2$ and Ge$_4$Se$_9$ based on KPFM and UPS measurement. c) Schematic of charge-trap mechanism applied positive back gate voltage through band diagram. d) Time-dependence of drain current under the change of V_{bg} from 30 to 80 V ranges with increasing 10 V (V_{ds} = 0.1 V). e) Extracted time constant (τ) shown in (b) by the fitting of exponential decay function. f) The change of ΔV_{th} at the temperature range 100–500 K within the range $V_{bg} = \pm 50$ V. The red dashed line denotes the exponential fits.

**ADVANCED
SCIENCE NEWS**

www.advancedsciencenews.com

**ADVANCED
MATERIALS**

www.advmat.de

electrons are then confined to the SiO$_2$ side of Ge$_4$Se$_9$ interface. In this case, there are two possible contributions, which affect charge transfer: thermionic emission and tunneling. Note that the conduction band offset (potential barrier height) between the MoS$_2$ and Ge$_4$Se$_9$ ($\approx$0.65 eV) is small enough for the electrons to be transferred over and then trapped at the interface of Ge$_4$Se$_9$/SiO$_2$ by thermionic emission (Figure 4c).

To determine the dominant contribution of the charge transfer, we designed a simple model and calculated the decay time using the following equation, which has been reported in previous studies:[9,10]

$$\tau = \frac{a}{vT} \tag{1}$$

where a is the thickness of MoS$_2$ and v and T are the average velocity of the electrons and the transmission coefficient, respectively. In particular, the transmission coefficient of the thermionic emission (T_{TH}) follows the Boltzmann factor, which is represented by:[9,10]

$$T_{\text{TH}} = \exp\left(-\frac{E_{\text{b}} - \varepsilon}{k_{\text{B}}T}\right) \tag{2}$$

where E_{b} is the potential barrier height between MoS$_2$ and Ge$_4$Se$_9$ ($\approx$0.65 eV), ε is the average energy of electrons, k_{B} is the Boltzmann constant, and T is the temperature (300 K) of the system. In terms of the transmission coefficient of tunneling, we referred to the Fowler–Nordheim (FN) tunneling mechanism, as shown in the following equation:[9,10,60,61]

$$T_{\text{FN}} = \exp\left(-\frac{4\sqrt{2m^*}}{3\hbar}\frac{(E_{\text{b}} - \varepsilon)^{3/2}}{eV_{\text{Ge}_4\text{Se}_9}}t\right) \tag{3}$$

where m^* is the effective mass of electron, $\hbar$ is the Plank constant, t is the thickness of Ge$_4$Se$_9$, and $V_{\text{Ge}_4\text{Se}_9}$ is the applied voltage to Ge$_4$Se$_9$ at a back-gate voltage level of +50 V. Note that T_{TH} is independent of the applied gate voltage, while T_{FN} is dependent on the applied gate voltage from the above equation. The calculated T_{TH} and T_{FN} are $\approx$3.78 × 10^{-11} and $\approx$1.16 × 10^{-17}, respectively (more details in Note SIV, Supporting Information). The difference between the T_{TH} and T_{FN} values was about six orders of magnitude, indicating that the thermionic emission held the dominant effect over the tunneling on the charge transfer between MoS$_2$ and Ge$_4$Se$_9$ in our vdW heterostructure. Additionally, from the value of T_{TH}, we can estimate the decay time of $\approx$1.26 s for the thermionic emission.

In order to experimentally confirm the charge transfer model of the MoS$_2$/Ge$_4$Se$_9$ vdW heterostructure device, we measured the time dependence of the current level by increasing the gate voltage from 30 to 80 V with 10 V steps (Figure 4d), followed by the time constant (τ) extraction through the fitting of the exponential decay function, as shown in Figure 4e. The extracted time constant was measured $\approx$1.5 s, regardless of the applied gate voltage, consistent with the calculated decay time for the thermionic emission (1.26 s). From the temperature dependence measurement of hysteresis behavior, as shown in Figure 4f, the ΔV_{th} exhibited an exponential increase from 100 to 500 K, following

the Boltzmann factor. Simultaneously, the drain ON current level gradually decreased (Figure S11, Supporting Information), which indicates that the electrons of MoS$_2$ were transferred more to Ge$_4$Se$_9$ at a high temperature. From all these results, we can conclude that the large hysteresis window of our MoS$_2$/Ge$_4$Se$_9$ vdW heterostructure device originates from the interfacial charge transfer based on the thermionic emission, owing to the low band offset of MoS$_2$/Ge$_4$Se$_9$ (of $\approx$0.65 eV). It is noteworthy that our MoS$_2$/Ge$_4$Se$_9$ vdW heterostructure device exhibits a lower conduction band offset compared to the other previous reports of the heterojunction between 2D semiconductors and wide-bandgap materials (Figure S12, Supporting Information).[9,10,55,62–66] Namely, in order for there to be a convenient charge transfer exerting a large hysteresis window, a suitable material configuration for low band offset should be required. In this regard, Ge$_4$Se$_9$ can possibly be a novel selection of 2D insulating material for the low-band offset formation of MoS$_2$ with a type I vdW heterostructure.

2.3. Potential for Artificial Synaptic Device Application

Thanks to the novel memristive performance of 2D-based memory devices, such as their low energy consumption, flexibility, and high integration, the utilization of 2D-based synaptic devices[67,68] has been reported in the last few years. Hence, we further investigate the potential use of the MoS$_2$/Ge$_4$Se$_9$ vdW heterostructure as a synaptic device based on the interfacial charge transfer (**Figure 5**a). One of the key factors of a synaptic device is the linear weight update operations, and many studies have reported that low non-linearity is required to achieve a high-performance neuromorphic system.[69,70]

In order to investigate the use of MoS$_2$/Ge$_4$Se$_9$ vdW heterostructure as a synaptic device, we applied voltage pulses at the back-gate terminal. Figure 5b reveals the gradual changes of post-synaptic current (PSC) at three different back-gate read voltages after applying 32 pulses (potentiation for −22 V with 1 ms and depression for +22 V with 1 ms). For over 2250 cycles, our device exhibited stable and linear conductance modulations for potentiation and depression behaviors. Indeed, in Figure 5c, we obtained the nonlinear values of 0.26 and 0.95 for potentiation and depression, respectively, from the following equations[70]

$$G_{\text{po}} = G_1\left(1 - e^{vP}\right) + G_{\text{min}}, \quad G_{\text{de}} = G_{\text{max}} - G_1\left(1 - e^{-v(P-1)}\right) \tag{4}$$

$$G_1 = \frac{G_{\text{max}} - G_{\text{min}}}{1 - e^{vP}} \tag{5}$$

where the v is the nonlinear value, P is the normalized pulse number, G_{max} is the maximum conductance, and G_{min} is the minimum conductance. We believe that the low non-linearity ($v < 1$) could originate from the interfacial charge transfer by the intrinsic low band offset of the MoS$_2$/Ge$_4$Se$_9$. This is because the electrons trapped between Ge$_4$Se$_9$ and SiO$_2$ are dominantly affected by the pulse-induced band bending of Ge$_4$Se$_9$. In other words, the number of trapped electrons is proportional to the applied pulse voltage. Indeed, the PSC was linearly increased when the pulse voltage was applied from −5 to −30 V, which indicates that the electrons trapped by pulse-dependent band bending are gradually released (Figure 5d).

**ADVANCED
SCIENCE NEWS**

www.advancedsciencenews.com

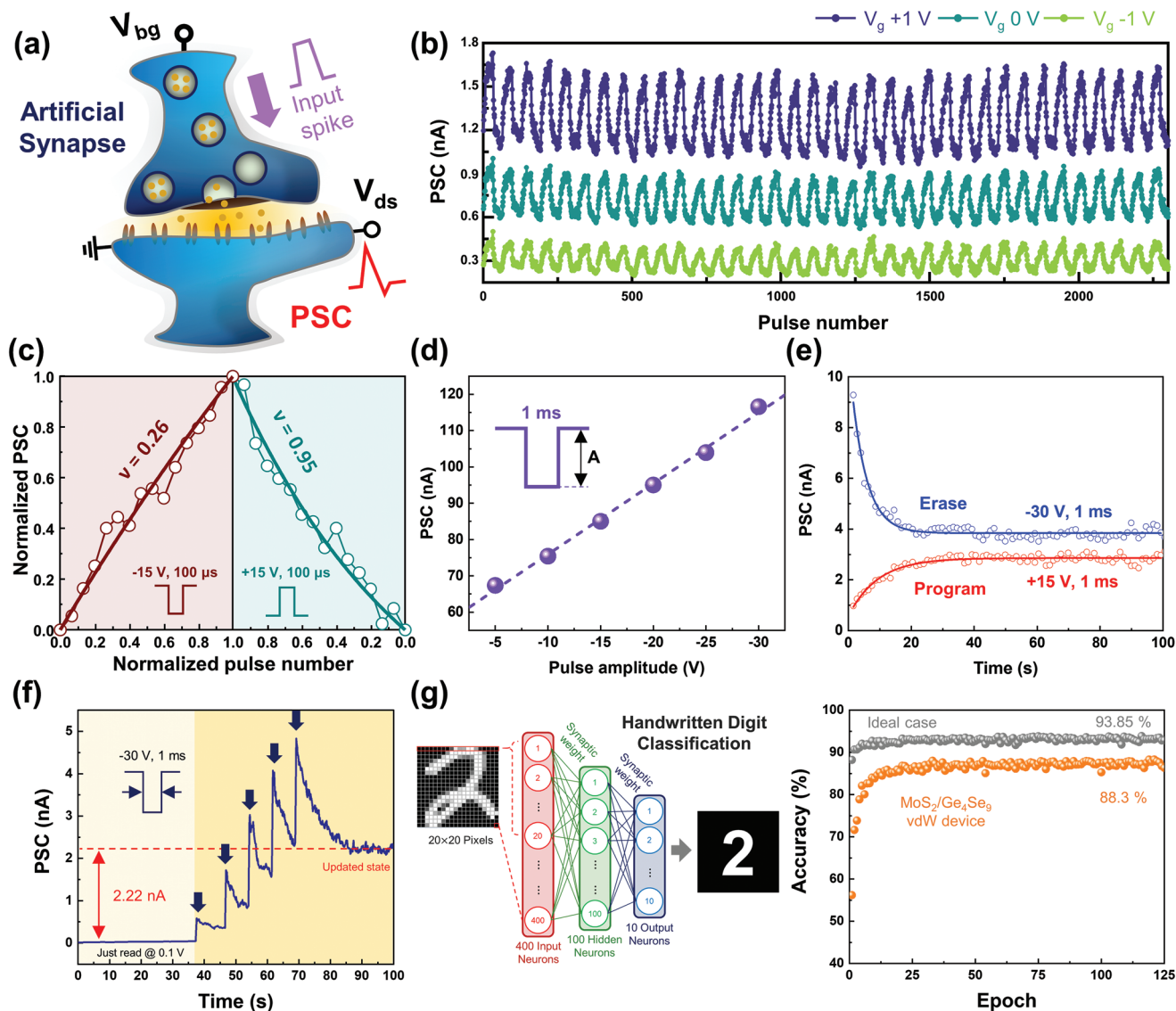**ADVANCED
MATERIALS**

www.advmat.de

Figure 5. Potential for emulating biological synapse. a) Illustration of the synaptic behavior by the artificial memtransistor using the gate terminal for pre-synapse, and source–drain terminal for post-synapse. b) The post-synaptic current (PSC) is modulated by the ±22 V pulse voltage with 1 ms width, corresponding to the potentiation and depression behavior within the 32 states. c) Non-linearity of potentiation and depression curve measured by applying the pulse with ±15 V amplitude and 100 µs width. d) Changes of PSC with incremental pulse amplitude from −5 to −30 V. e) Retention characteristics of programmed and erased states at $V_{bg} = 0$ V and $V_{ds} = 0.1$ V after applied pulse of +15 and −30 V, 1 ms. f) Time dependence of PSC under the applied five pulses (amplitude; −30 V, 1 ms width, 10 s period). g) MNIST handwritten image classification and the accuracy by setting ideal of parameters and the MoS_2/Ge_4Se_9 vdW device.

The energy consumption for our MoS_2/Ge_4Se_9 synaptic device was estimated to be approximately 15 fJ for updating energy and 40 fJ for reading energy, using the following equation[71,72]

$$E = V_{spike} \times I \times t_{duration} \qquad (6)$$

where V_{spike} is the amplitude of update and read spike, I is the current of each operation mode, and $t_{duration}$ is the duration of update and read spike, respectively (Figure S13, Supporting Information).

The retention characteristics of programmed and erased states were measured as shown in Figure 5e. We applied +15

and −30 V with 1 ms pulses in order to set initially programmed and erased states and observed a time-dependent conductance change of each state at $V_{ds} = 0.1$ V with $V_{bg} = 0$ V. During the first few seconds, the programmed and erased states dramatically decayed, and then they entered in saturation states while maintaining their conductance levels. According to the interfacial charge transfer based on thermionic emission, the programmed and erased states should ideally be returned to the same conductance state, as there is no gate voltage that induces a charge transfer. However, interestingly, we obtained separated conductance saturation levels after the program and erase pulses were applied, thus indicating the presence of synaptic

**ADVANCED
SCIENCE NEWS**

www.advancedsciencenews.com

**ADVANCED
MATERIALS**

www.advmat.de

long-term plasticity behavior. In order to understand this long-term plasticity, we fitted erased states with a biexponential function and extracted two decay time constants of $\tau_1 = 2.5$ s and $\tau_2 = 9.2$ s. From the two different time constants, we assumed that the transferred charges were partially trapped within the Ge and Se vacancies of Ge_4Se_9, which can occur under Se-rich growth conditions.[73] According to previous reports,[9,74] the shorter time constant τ_1 could be affected by the charge transfer, while the longer time constant τ_2 could be related to the vacancies at the body of Ge_4Se_9. This is due to the vacancy energy states present within Ge_4Se_9 bandgap having a higher potential barrier than the conduction band offset of the heterostructure. The presence of both short-term and long-term characteristics was still maintained after applying multiple pulses. Figure 5f shows the time-dependence of PSC after 5 pulses with 1 ms width and 10 s period for each pulse when the decay process was progressed considerably. After five consecutive pulses were applied, the saturated PSC clearly exhibits a different state from the original state. Moreover, both the excitatory and inhibitory states of the long-term plasticity were obtained for 1000 s (Figure S14, Supporting Information). Thus, our MoS_2/Ge_4Se_9 vdW heterostructure device exhibited both volatile (short-time decay in the subsecond range) and nonvolatile (long-term plasticity after a few seconds) behaviors that can be further exploited in artificial learning systems, such as associative learning.[41,42,52]

Finally, we performed the MNIST handwritten image classification in order to expand the utility of the Ge_4Se_9 synaptic device. The multilayer perceptron (MLP) simulation was designed by the two-layer of MLP neural network consisted of 400 input neurons (MNIST handwritten image; 20×20 pixels), one hidden layer with 100 neurons (the simplified input features based on synaptic weight matrix), and ten output neurons (corresponding to the numbers from 0 to 9) as shown in Figure 5g. Each layer of neurons was fully connected by the synapses, and the weights of synapses were updated through the feed-forward and back-propagation processes.[69,75–78] The device parameters for the synaptic array in the simulation were selected from the several PD curves (80 states) measurement results with relatively high dynamic range (G_{max}/G_{min}) of around 4 with low linearity. For the neural network training, each epoch used 8000 images randomly selected from 60 000 training data set by using the Adam algorithm. After the training, the image classification accuracy was evaluated by 10 000 images from the test data set. As shown in Figure 5g, the learning accuracy was achieved and reached a maximum of 88.3% (average of 86.17%), which is comparable to the 93.85% of the ideal case.

3. Conclusion

We have successfully developed a new 2D material growth method, specifically for 2D-layered Ge_4Se_9. We expect that the precursor engineering that we used to grow 2D-layered Ge_4Se_9 could provide a general route to achieve a new 2DLM. Furthermore, owing to the non-dangling bond of 2D materials, the configuration of the vdW heterostructure with semiconductor and insulator has been one of the most attractive candidates exhib-

iting high device performance, such as mobility, subthreshold swing, and memory window. In this regard, Ge_4Se_9 offers a new type of 2D insulating material family by offering various heterostructure configurations. Specifically, due to the intrinsic low-conduction band offset, the MoS_2/Ge_4Se_9 vdW heterostructure device exhibits a large hysteresis window (129 V at ±80 V back-gate sweep) with linear gate-tunability and also applicability to a synaptic device with low non-linearity ($\nu_{po} = 0.26$ and $\nu_{de} = 0.95$), the low energy consumption (15 fJ for updating energy), and also high learning accuracy (88.3%). Therefore, we believe that Ge_4Se_9 can provide remarkable opportunities for band offset-related applications, in addition to neuromorphic research.

4. Experimental Section

MOCVD Growth of $GeSe_2$ and Ge_4Se_9: The $GeSe_2$ and Ge_4Se_9 flakes were grown by the MOCVD process, and a tube furnace with a tube diameter of 2 inches was used. Additionally, $Ge(dmamp)_2$ and $(CH_3)_2Se$ were used as Ge and Se precursors, respectively. $(CH_3)_2Se$ was kept in a bubbler system at a constant pressure of 800 Torr, and Ar was used as the carrier gas. Due to the relatively low vapor pressure, $Ge(dmamp)_2$ was directly injected into the inlet of the tube by inserting with Ar gas. The canister that contained $Ge(dmamp)_2$ was kept at 45 °C with the use of heating tape, and the line from the canister to the inlet was also heated. The flow rate was precisely controlled by Mass flow controller. The optimum flow rate of precursor was 60 sccm for $Ge(dmamp)_2$, 0.6 sccm for $(CH_3)_2Se$, 180 sccm for Ar, and 5 sccm for H_2, with H_2 also being used to eliminate carbon residue. The tube furnace consisted of two heating zones, and the precursors were decomposed in the first heating zone. The growth of Ge_4Se_9 took place in the second heating zone. Freshly cleaved muscovite mica substrates were placed at the start of the second heating zone, and both heating zones were heated to $T_1 = 480$ °C and $T_2 = 240$ °C (or 400 °C for $GeSe_2$) for 30 min with Ar 50 sccm and H_2 10 sccm, with their temperatures maintained during the growth time, and the pressure continuously maintained at around ≈300–400 Torr.

Transfer and Device Fabrication Method: The transfer was done using PDMS and PC. The PC was dissolved in chloroform at a concentration of 5 wt%. The PC was spin-coated at 4000 rpm for 30 s on a mica substrate with Ge_4Se_9 flakes. The PC-coated mica edge was cut with a razor blade to allow water to penetrate effectively in a later step. PDMS was attached to the PC-coated mica substrate to assist the PC films. Afterward, the distilled water was injected by pipette to the side of the sample (PDMS/PC/Ge_4Se_9/mica). This weakened the adhesive force between mica and the PC/Ge_4Se_9 layer, so the PDMS/PC/Ge_4Se_9 layer to be peeled off from the mica substrate. To attach the sample to the target substrate, the heat was applied to 150 °C while pressing, and the PDMS was then peeled off. PC film was removed through immersion in chloroform, acetone, and IPA, in sequence. In order to fabricate the bottom gate MoS_2/Ge_4Se_9 vdW heterostructure device, exfoliated MoS_2 was used, and Ge_4Se_9 flakes were transferred by way of PDMS/PC-based transfer, and SiO_2 (300 nm)/Si (n^{++}) substrate was used. The source and drain were patterned using e-beam lithography (VEGA3 LMH Elphy Quantum Lithography System), and Cr 10 nm Au 40 nm was deposited by e-beam evaporator (SNTEK).

Characterization and Electrical Measurements: Optical microscopy (Olympus) was used to characterize the morphology of Ge_4Se_9. Atomic force microscopy (AFM) (Innova-Labram HR800) with the tapping mode was then used to further characterize the morphology and measure the thickness of Ge_4Se_9 flakes. XRD (SmartLab) pattern was obtained with Cu–$K\alpha$ radiation in order to identify the phase and crystallinity. TEM (Titan Cube G2 60–300, Thermo Fisher Scientific) characterization was performed to obtain the SAED pattern, STEM images, and EDX spectrum. Through XPS analysis (Axis-Supra), an atomic bonding state

was obtained. In order to get the Raman spectrum, Raman spectrometry (ARAMIS) was applied with the 514 nm laser. All electrical measurements of the fabricated devices were performed by Keithley 4200A-SCS. Finally, the work function was measured by KPFM with Pt/Ir coated Si tip at the ambient condition. In order to prevent contact with the step of the sample, the scanning process was completed in very low speed mode ($\approx$0.1 Hz)

DFT Calculation Method: The density-functional theory (DFT) calculations were performed as implemented in the Vienna Ab initio Simulation Package (VASP) code.[79] The projector-augmented wave pseudopotentials[80,81] and a kinetic energy cutoff of 500 eV were applied. The Perdew, Burke, and Ernzerhof functional within the generalized gradient approximation was used for the exchange correlation functional.[82] The long-range van der Waals interaction was described with the vdW-D2 corrections proposed by Grimme in phonon calculations.[83,84] The primitive 52-atomic orthorhombic unit cell of Ge_4Se_9 with a Γ-centered $2 \times 5 \times 3$ k-point mesh and the primitive 48-atomic monoclinic unit cell of $GeSe_2$ with a Γ-centered $5 \times 2 \times 3$ k-point mesh were used for the Brillouin zone (BZ) summation. The Hellmann–Feynman forces were relaxed to lower than 0.001 eV Å^{-1}. For the band structure calculation, the hybrid functional of Heyd–Scuseria–Ernzerhof, with a mixing parameter of 0.25 and a screening parameter of 0.2 Å^{-1}, was used for the exchange–correlation energy of the electrons.[85] The phonon calculations were performed using Phonopy code.[86] The dynamical matrix was constructed using the finite-difference method with the Hellmann−Feynman forces calculated within $1 \times 2 \times 1$ supercell for Ge_4Se_9 and $2 \times 1 \times 1$ supercell for $GeSe_2$. The total energies were minimized in self-consistent calculations to lower than 10^{-8} eV in order to obtain a high accuracy of the forces. In thermodynamic calculations, an Γ-centered $6 \times 12 \times 6$ q-point mesh for Ge_4Se_9 and a Γ-centered $12 \times 6 \times 6$ q-point mesh for $GeSe_2$ were used for the BZ summation.

Supporting Information

Supporting Information is available from the Wiley Online Library or from the author.

Conflict of Interest

The authors declare no conflict of interest.

Data Availability Statement

The data that support the findings of this study are available on request from the corresponding author. The data are not publicly available due to privacy or ethical restrictions.

[1] A. K. Geim, I. V. Grigorieva, *Nature* **2013**, *499*, 419.
[2] Y. Liu, N. O. Weiss, X. Duan, H.-C. Cheng, Y. Huang, X. Duan, *Nat. Rev. Mater.* **2016**, *1*, 16042.
[3] D. Jariwala, T. J. Marks, M. C. Hersam, *Nat. Mater.* **2017**, *16*, 170.
[4] K. S. Burch, D. Mandrus, J. G. Park, *Nature* **2018**, *563*, 47.
[5] Z. Lin, Y. Huang, X. Duan, *Nat. Electron.* **2019**, *2*, 378.
[6] S. J. Liang, B. Cheng, X. Cui, F. Miao, *Adv. Mater.* **2020**, *32*, 1903800.
[7] J. F. Sierra, J. Fabian, R. K. Kawakami, S. Roche, S. O. Valenzuela, *Nat. Nanotechnol.* **2021**, *16*, 856.
[8] Y. Jiang, S. Chen, W. Zheng, B. Zheng, A. Pan, *Light: Sci. Appl.* **2021**, *10*, 72.
[9] A. S. Kumar, M. Wang, Y. Li, R. Fujita, X. P. A. Gao, *ACS Appl. Mater. Interfaces* **2020**, *12*, 46854.
[10] J. Yao, W. Guo, Y. Liu, X. Niu, M. Li, X. Wu, Y. Yu, T. Ou, J. Sha, Y. Wang, *J. Mater. Chem. C* **2021**, *9*, 8213.
[11] Y. Cao, V. Fatemi, S. Fang, K. Watanabe, T. Taniguchi, E. Kaxiras, P. Jarillo-Herrero, *Nature* **2018**, *556*, 43.
[12] N. Mounet, M. Gibertini, P. Schwaller, D. Campi, A. Merkys, A. Marrazzo, T. Sohier, I. E. Castelli, A. Cepellotti, G. Pizzi, N. Marzari, *Nat. Nanotechnol.* **2018**, *13*, 246.
[13] R. Liu, F. Wang, L. Liu, X. He, J. Chen, Y. Li, T. Zhai, *Small Struct.* **2020**, *2*, 2000041.
[14] Q. Wang, L. Zhang, X. Liu, S. Li, *Front. Energy Res.* **2021**, *9*, 802055.
[15] X. Wang, P. Yu, Z. Lei, C. Zhu, X. Cao, F. Liu, L. You, Q. Zeng, Y. Deng, C. Zhu, J. Zhou, Q. Fu, J. Wang, Y. Huang, Z. Liu, *Nat. Commun.* **2019**, *10*, 3037.
[16] W. Shi, S. Kahn, L. Jiang, S.-Y. Wang, H.-Z. Tsai, D. Wong, T. Taniguchi, K. Watanabe, F. Wang, M. F. Crommie, A. Zettl, *Nat. Electron.* **2020**, *3*, 99.
[17] M. M. Obeid, A. Bafekry, S. Ur Rehman, C. V. Nguyen, *Appl. Surf. Sci.* **2020**, *534*, 147607.
[18] J. Kwon, J. C. Shin, H. Ryu, J. Y. Lee, D. Seo, K. Watanabe, T. Taniguchi, Y. D. Kim, J. Hone, C. H. Lee, G. H. Lee, *Adv. Mater.* **2020**, *32*, 2003567.
[19] K. Yang, S. Wang, T. Han, H. Liu, *Nanomaterials* **2021**, *11*, 1971.
[20] X. Pan, Y. Zheng, Y. Shi, W. Chen, *ACS Mater. Lett.* **2021**, *3*, 235.
[21] M. Akazawa, T. Matsuyama, T. Hashizume, M. Hiroki, S. Yamahata, N. Shigekawa, *Appl. Phys. Lett.* **2010**, *96*, 132104.
[22] A. Panchak, A. Luque, A. Vlasov, A. Andreev, A. Martí, *Sol. Energy Mater. Sol. Cells* **2016**, *145*, 180.
[23] C. Ding, Y. Zhang, F. Liu, Y. Kitabatake, S. Hayase, T. Toyoda, K. Yoshino, T. Minemoto, K. Katayama, Q. Shen, *Nano Energy* **2018**, *53*, 17.
[24] W. Hu, H. Cong, W. Huang, Y. Huang, L. Chen, A. Pan, C. Xue, *Light: Sci. Appl.* **2019**, *8*, 106.
[25] X. Zhou, Q. Zhang, L. Gan, H. Li, J. Xiong, T. Zhai, *Adv. Sci.* **2016**, *3*, 1600177.
[26] Y. Lu, J. H. Warner, *ACS Appl. Electron. Mater.* **2020**, *2*, 1777.
[27] R. Woods-Robinson, Y. Han, H. Zhang, T. Ablekim, I. Khan, K. A. Persson, A. Zakutayev, *Chem. Rev.* **2020**, *120*, 4007.
[28] X. Zhou, X. Hu, S. Zhou, Q. Zhang, H. Li, T. Zhai, *Adv. Funct. Mater.* **2017**, *27*, 1703858
[29] X. Hu, P. Huang, K. Liu, B. Jin, X. Zhang, X. Zhang, X. Zhou, T. Zhai, *ACS Appl. Mater. Interfaces* **2019**, *11*, 23353.

**ADVANCED
SCIENCE NEWS**

www.advancedsciencenews.com

**ADVANCED
MATERIALS**

www.advmat.de

[30] Z. Wang, M. Li, X. P. A. Gao, Z. Zhang, *ACS Appl. Electron. Mater.* **2019**, *1*, 2236.

[31] K. Yumigeta, C. Brayfield, H. Cai, D. Hajra, M. Blei, S. Yang, Y. Shen, S. Tongay, *RSC Adv.* **2020**, *10*, 38227.

[32] G. Guo, Y. Shi, Y. Zhang, Y. Deng, F. Du, Z. Xie, J. Tang, Y. Mao, *Comput. Mater. Sci.* **2020**, *172*, 109348.

[33] H. Yu, D. Gao, X. Wang, X. Du, X. Lin, W. Guo, R. Zou, C. Jin, K. Li, Y. Chen, *NPG Asia Mater.* **2018**, *10*, 882.

[34] Z. Guan, Y. Zhao, X. Wang, N. Zhong, X. Deng, Y. Zheng, J. Wang, D. Xu, R. Ma, F. Yue, Y. Cheng, R. Huang, P. Xiang, Z. Wei, J. Chu, C. Duan, *ACS Nano* **2022**, *16*, 1308.

[35] X. Zhang, J. Shen, S. Lin, J. Li, Z. Chen, W. Li, Y. Pei, *J. Materiomics* **2016**, *2*, 331.

[36] J. Tang, F. Zhang, F. Zhou, X. Tang, X. Dai, S. Lu, *Nanophotonics* **2020**, *9*, 2007.

[37] C. He, J. H. Zhang, W. X. Zhang, T. T. Li, *J. Phys. Chem. C* **2019**, *123*, 5157.

[38] K. Ren, M. Zhu, W. Song, S. Lv, M. Xia, Y. Wang, Y. Lu, Z. Ji, Z. Song, *Nanoscale* **2019**, *11*, 1595.

[39] A. M. Afzal, M. Z. Iqbal, S. Mumtaz, I. Akhtar, *J. Mater. Chem. C* **2020**, *8*, 4743.

[40] H. Lee, S. W. Cho, S. J. Kim, J. Lee, K. S. Kim, I. Kim, J.-K. Park, J. Y. Kwak, J. Kim, J. Park, Y. Jeong, G. W. Hwang, K.-S. Lee, D. Ielmini, S. Lee, *Nano Lett.* **2022**, *22*, 733.

[41] M. Yan, Q. Zhu, S. Wang, Y. Ren, G. Feng, L. Liu, H. Peng, Y. He, J. Wang, P. Zhou, X. Meng, X. Tang, J. Chu, B. Dkhil, B. Tian, C. Duan, *Adv. Electron. Mater.* **2021**, *7*, 2001276.

[42] X. Ji, B. D. Paulsen, G. K. K. Chik, R. Wu, Y. Yin, P. K. L. Chan, J. Rivnay, *Nat. Commun.* **2021**, *12*, 2480.

[43] H. Fjellvåg, K. O. Kongshaug, S. Stølen, *J. Chem. Soc., Dalton Trans.* **2001**, 1043.

[44] J. E. Kwak, H. Yun, *Acta Crystallogr. C* **2005**, *61*, i81.

[45] J. K. Das, A. K. Samantara, A. S. K. , C. S. Rout, J. N. Behera, *Dalton Trans.* **2019**, *48*, 15955.

[46] H.-S. Kim, E. A. Jung, S. H. Han, J. H. Han, B. K. Park, C. G. Kim, T.-M. Chung, *Inorg. Chem.* **2017**, *56*, 4084.

[47] J. M. Hwang, J. H. Lee, H.-S. Kim, C. W. Park, D. Yoo, B. K. Park, C. G. Kim, T.-M. Chung, *Polyhedron* **2020**, *176*, 114289.

[48] Y. Zhao, J.-G. Song, G. H. Ryu, K. Y. Ko, W. J. Woo, Y. Kim, D. Kim, J. H. Lim, S. Lee, Z. Lee, J. Park, H. Kim, *Nanoscale* **2018**, *10*, 9338.

[49] A. Kozhakhmetov, R. Torsi, C. Y. Chen, J. A. Robinson, *J. Phys.: Mater.* **2020**, *4*, 012001.

[50] J. K. Jeong, H. Won Yang, J. H. Jeong, Y.-G. Mo, H. D. Kim, *Appl. Phys. Lett.* **2008**, *93*, 123508.

[51] W. Feng, W. Zheng, X. Chen, G. Liu, P. Hu, *ACS Appl. Mater. Interfaces* **2015**, *7*, 26691.

[52] G. Ding, B. Yang, R. S. Chen, W. A. Mo, K. Zhou, Y. Liu, G. Shang, Y. Zhai, S. T. Han, Y. Zhou, *Small* **2021**, *17*, e2103175.

[53] Y. Guo, X. Wei, J. Shu, B. Liu, J. Yin, C. Guan, Y. Han, S. Gao, Q. Chen, *Appl. Phys. Lett.* **2015**, *106*, 103109.

[54] M. Chen, Y. Wang, N. Shepherd, C. Huard, J. Zhou, L. J. Guo, W. Lu, X. Liang, *ACS Nano* **2017**, *11*, 1091.

[55] J. H. Nam, S. Oh, H. Y. Jang, O. Kwon, H. Park, W. Park, J.-D. Kwon, Y. Kim, B. Cho, *Adv. Funct. Mater.* **2021**, *31*, 2104174.

[56] M. Shin, M. J. Lee, C. Yoon, S. Kim, B. H. Park, S. Lee, J.-G. Park, *J. Korean Phys. Soc.* **2021**, *78*, 816.

[57] J. Shu, G. Wu, Y. Guo, B. Liu, X. Wei, Q. Chen, *Nanoscale* **2016**, *8*, 3049.

[58] A. J. Arnold, A. Razavieh, J. R. Nasr, D. S. Schulman, C. M. Eichfeld, S. Das, *ACS Nano* **2017**, *11*, 3110.

[59] Q. Xu, Y. Sun, P. Yang, Y. Dan, *AIP Adv.* **2019**, *9*, 015230.

[60] M. Depas, B. Vermeire, P. W. Mertens, R. L. Van Meirhaeghe, M. M. Heyns, *Solid-State Electron.* **1995**, *38*, 1465.

[61] K. F. Mak, C. Lee, J. Hone, J. Shan, T. F. Heinz, *Phys. Rev. Lett.* **2010**, *105*, 136805.

[62] V. V. Afanas'ev, D. Chiappe, C. Huyghebaert, I. Radu, S. De Gendt, M. Houssa, A. Stesmans, *Microelectron. Eng.* **2015**, *147*, 294.

[63] M. Tangi, P. Mishra, T. K. Ng, M. N. Hedhili, B. Janjua, M. S. Alias, D. H. Anjum, C.-C. Tseng, Y. Shi, H. J. Joyce, L.-J. Li, B. S. Ooi, *Appl. Phys. Lett.* **2016**, *109*, 032104.

[64] Y. Chen, S. Huang, X. Ji, K. Adepalli, K. Yin, X. Ling, X. Wang, J. Xue, M. Dresselhaus, J. Kong, B. Yildiz, *ACS Nano* **2018**, *12*, 2569.

[65] Q. Zhang, S. Zhang, B. A. Sperling, N. V. Nguyen, *J. Electron. Mater.* **2019**, *48*, 6446.

[66] L. Liu, C. Liu, L. Jiang, J. Li, Y. Ding, S. Wang, Y. G. Jiang, Y. B. Sun, J. Wang, S. Chen, D. W. Zhang, P. Zhou, *Nat. Nanotechnol.* **2021**, *16*, 874.

[67] W. Huh, D. Lee, C.-H. Lee, *Adv. Mater.* **2020**, *32*, 2002092.

[68] C.-Y. Wang, C. Wang, F. Meng, P. Wang, S. Wang, S.-J. Liang, F. Miao, *Adv. Electron. Mater.* **2020**, *6*, 1901107.

[69] P. Chen, X. Peng, S. Yu, *IEEE Trans. Comput.-Aided Des. Integr. Circuits Syst.* **2018**, *37*, 3067.

[70] S. Agarwal, S. J. Plimpton, D. R. Hughart, A. H. Hsia, I. Richter, J. A. Cox, C. D. James, M. J. Marinella, in *2016 Int. Joint Conf. on Neural Networks (IJCNN)*, IEEE, Piscataway, NJ, USA **2016**, pp. 929–938.

[71] S. Seo, J.-J. Lee, H.-J. Lee, H. W. Lee, S. Oh, J. J. Lee, K. Heo, J.-H. Park, *ACS Appl. Electron. Mater.* **2020**, *2*, 371.

[72] S. Seo, B.-S. Kang, J.-J. Lee, H.-J. Ryu, S. Kim, H. Kim, S. Oh, J. Shim, K. Heo, S. Oh, J.-H. Park, *Nat. Commun.* **2020**, *11*, 3936.

[73] S. Zhang, M. L. Li, M. Jiang, H. Xiao, D. O. Scanlon, X. Zu, *J. Phys. B: At., Mol. Opt. Phys.* **2021**, *54*, 035003.

[74] D. Lynall, S. V. Nair, D. Gutstein, A. Shik, I. G. Savelyev, M. Blumin, H. E. Ruda, *Nano Lett.* **2018**, *18*, 1387.

[75] D.-H. Kang, J.-H. Kim, S. Oh, H.-Y. Park, S. R. Dugasani, B.-S. Kang, C. Choi, R. Choi, S. Lee, S. H. Park, K. Heo, J.-H. Park, *Adv. Sci.* **2019**, *6*, 1901265.

[76] S.-K. Lee, Y. W. Cho, J.-S. Lee, Y.-R. Jung, S.-H. Oh, J.-Y. Sun, S. Kim, Y.-C. Joo, *Adv. Sci.* **2021**, *8*, 2001544.

[77] S. Li, M.-E. Pam, Y. Li, L. Chen, Y.-C. Chien, X. Fong, D. Chi, K.-W. Ang, *Adv. Mater.* **2022**, *34*, 2103376.

[78] L. Wang, X. Wang, Y. Zhang, R. Li, T. Ma, K. Leng, Z. Chen, I. Abdelwahab, K. P. Loh, *Adv. Funct. Mater.* **2020**, *30*, 2004609.

[79] G. Kresse, J. Furthmüller, *Phys. Rev. B* **1996**, *54*, 11169.

[80] P. E. Blöchl, *Phys. Rev. B* **1994**, *50*, 17953.

[81] G. Kresse, D. Joubert, *Phys. Rev. B* **1999**, *59*, 1758.

[82] J. P. Perdew, K. Burke, M. Ernzerhof, *Phys. Rev. Lett.* **1996**, *77*, 3865.

[83] S. Grimme, J. Antony, S. Ehrlich, H. Krieg, *J. Chem. Phys.* **2010**, *132*, 154104.

[84] S. Grimme, S. Ehrlich, L. Goerigk, *J. Comput. Chem.* **2011**, *32*, 1456.

[85] J. Heyd, G. E. Scuseria, M. Ernzerhof, *J. Chem. Phys.* **2003**, *118*, 8207.

[86] F. Kirchhoff, G. Kresse, M. J. Gillan, *Phys. Rev. B* **1998**, *57*, 10482.